

2020

## Electron Tunneling and X-Ray Photoelectron Spectroscopy Studies of the Superconducting Properties of Nitrogen-Doped Niobium Resonator Cavities

Eric M. Lechner

Basu Dev Oli

Junki Makita

Old Dominion University, [jmaki002@odu.edu](mailto:jmaki002@odu.edu)

Gianluigi Ciovati

Old Dominion University, [gciovati@odu.edu](mailto:gciovati@odu.edu)

Alex Gurevich

Old Dominion University, [gurevich@odu.edu](mailto:gurevich@odu.edu)

*See next page for additional authors*

Follow this and additional works at: [https://digitalcommons.odu.edu/physics\\_fac\\_pubs](https://digitalcommons.odu.edu/physics_fac_pubs)



Part of the [Materials Science and Engineering Commons](#), and the [Physics Commons](#)

---

### Original Publication Citation

Lechner, E. M., Oli, B. D., Makita, J., Ciovati, G., Gurevich, A., & Iavarone, M. (2020). Electron tunneling and x-ray photoelectron spectroscopy studies of the superconducting properties of nitrogen-doped niobium resonator cavities. *Physical Review Applied*, 13(4), 044044. doi:10.1103/PhysRevApplied.13.044044

This Article is brought to you for free and open access by the Physics at ODU Digital Commons. It has been accepted for inclusion in Physics Faculty Publications by an authorized administrator of ODU Digital Commons. For more information, please contact [digitalcommons@odu.edu](mailto:digitalcommons@odu.edu).

---

**Authors**

Eric M. Lechner, Basu Dev Oli, Junki Makita, Gianluigi Ciovati, Alex Gurevich, and Maria Iavarone


# Electron Tunneling and X-Ray Photoelectron Spectroscopy Studies of the Superconducting Properties of Nitrogen-Doped Niobium Resonator Cavities

Eric M. Lechner,<sup>1</sup> Basu Dev Oli,<sup>1</sup> Junki Makita<sup>①</sup>,<sup>2</sup> Gianluigi Ciovati,<sup>3,2</sup> Alex Gurevich,<sup>2</sup> and Maria Iavarone<sup>①,1,\*</sup>

<sup>1</sup>*Department of Physics, Temple University, Philadelphia, Pennsylvania 19122, USA*

<sup>2</sup>*Department of Physics and Center for Accelerator Science, Old Dominion University, Norfolk, Virginia 23529, USA*

<sup>3</sup>*Thomas Jefferson National Accelerator Facility, Newport News, Virginia 23606, USA*

 (Received 19 July 2019; revised manuscript received 19 December 2019; accepted 23 March 2020; published 16 April 2020)

We use scanning tunneling microscopy (STM) and spectroscopy (STS), and x-ray photoelectron spectroscopy (XPS) to investigate the effect of nitrogen doping on the surface electronic and chemical structures of cutouts from superconducting Nb radio-frequency cavities. The goal of this work is to get insights into the fundamental physics and materials mechanisms behind the striking decrease of the surface resistance with the radio-frequency magnetic field, which has been observed on *N*-doped Nb cavities. Our XPS measurements reveal significantly more oxidized Nb 3*d* states and a thinner metallic suboxide layer on the *N*-doped Nb surfaces, which is also confirmed by tunneling spectroscopy measurements. In turn, tunneling measurements performed on native surfaces as well as on Ar-ion sputtered surfaces allow us to separate the effect of *N* doping on the surface-oxide layer from that on the density of states in the bulk. Analysis of our tunneling spectra in the framework of a model of a proximity-coupled normal layer at the surface [A. Gurevich and T. Kubo, Phys. Rev. B **96**, 184515 (2017)] is consistent with the hypothesis that *N*-doping ameliorates lateral inhomogeneities of superconducting properties on the surface and shrinks the metallic suboxide layer. For the Ar sputtered surfaces, we also find evidence that *N* doping changes the contact resistance between the metallic suboxide and the bulk niobium toward an optimum value corresponding to a minimum surface resistance. The totality of our experimental data suggests that the *N* doping provides an effective tuning of the density of states in such a way that it can result in a decrease of the surface resistance with the radio-frequency field, as predicted by calculations of the nonlinear low-frequency electromagnetic response of dirty superconductors. Furthermore, STM imaging of vortex cores shows a slightly reduced average superconducting gap and a shorter coherence length in the *N*-doped Nb samples as compared to typically prepared Nb samples, indicating a stronger impurity scattering caused by nitrogen doping in a moderately disordered material.

DOI: [10.1103/PhysRevApplied.13.044044](https://doi.org/10.1103/PhysRevApplied.13.044044)

## I. INTRODUCTION

The fundamental limits of dissipation in the superconducting Meissner state under rf fields has attracted much attention, particularly in light of recent advances in the improvement of the performance of microresonators for quantum computing or resonator cavities for particle accelerators [1–7]. This interest has been motivated by the fact that *s*-wave superconductors have very small surface resistance  $R_s \propto \exp(-\Delta/T)$  at temperatures  $T$  well below the critical temperature  $T_c$  and rf frequencies  $\omega$  smaller than the gap frequency  $2\Delta/\hbar$  [8]. Indeed, the Nb cavities typically have  $R_s \sim 10$  n $\Omega$  at 2 K and 1 GHz, which translates into huge quality factors  $Q \propto 1/R_s \sim 10^{10}$ – $10^{11}$  [4,5,7].

The surface resistance depends on the amplitude  $H_0$  of the rf magnetic field  $H(t) = H_0 \sin \omega t$  and can be significantly altered by the materials treatments. For instance,  $R_s$  of electropolished Nb cavities [4] at 2 K and 1 GHz increases with the rf-field amplitude, consistent with the well-known reduction of a quasiparticle gap and the superfluid density by the rf pairbreaking currents [9–11], grain boundaries, nonsuperconducting precipitates, and other materials defects [5,12], or trapped vortices [13–21]. However, the Nb cavities doped with nitrogen [22–25], titanium [26], or other impurities [27,28] can exhibit a striking reduction of  $R_s(H_0)$  by factors of 2–4 as  $H_0$  increases from 0 to  $\lesssim 0.5H_c$ , where  $H_c$  is the thermodynamic critical field.

These discoveries of the microwave reduction of  $R_s(H_0)$  have triggered intense investigations of its microscopic mechanisms, as well as the materials modifications

\*iavarone@temple.edu

[29–34], by which it can be further enhanced and extended to higher rf fields of prime importance for the superconducting rf- (SRF) cavity applications. The investigations indicate that the behavior of the nonlinear surface resistance at high rf fields is controlled by the physics of nonequilibrium superconductivity and nonlinear rf current pairbreaking interconnected with subtle materials features and impurity distributions in the first few nm at the surface. One of the outstanding issues is to understand the mechanism by which the impurity doping turns the conventional increase of  $R_s(H_0)$  with  $H_0$  into the counterintuitive decrease of  $R_s(H_0)$  as a function of  $H_0$ . Several scenarios for this effect have been proposed in the literature. It was shown [35] that the well-known effect of broadening the gap peaks of the quasiparticle density of states (DOS) by the pairbreaking current [9,10,36–40] can result in a pronounced minimum in  $R_s(H_0)$ , in agreement with experiment [25,26]. Such a microwave reduction of the surface resistance [41] is a manifestation of a general effect by which  $R_s$  can be significantly reduced by engineering an optimum broadening of the gap peaks in the DOS at the surface using different *pairbreaking* mechanisms. These mechanisms can be due to rf Meissner currents [35,40,41], paramagnetic impurities [42,43], local reduction of the pairing constant, or a proximity-coupled normal layer, which models surface nonstoichiometry and suboxide layers [44,45]. The latter are particularly relevant to the Nb surface, which is typically covered by a few-nm-thick layers of metallic Nb monoxide (NbO), semiconducting Nb dioxide (NbO<sub>2</sub>), and insulating Nb pentoxide (Nb<sub>2</sub>O<sub>5</sub>) [5,46,47]. Low-oxidation-state Nb suboxides tend to be metallic with known magnetic moments appearing as the oxide approaches the Nb<sup>4+</sup> state [48–50]. Another mechanism of the field reduction of  $R_s(H_0)$  based on the existence of two-level atomic states at the Nb surface was proposed [51] although neither the nature of the two-level atomic states nor their relation to the  $N$  doping of Nb cavities have been well understood. Recently, a contribution to a negative  $Q(H_0)$  slope coming from trapped vortices was suggested [52].

Identifying the materials and physical mechanisms by which the  $N$  doping causes the field-induced reduction of  $R_s(H_0)$  requires surface probes that can pinpoint the specific superconducting properties affected by the  $N$  doping. In turn, these experiments should be combined with a theory that relates these materials changes to the corresponding changes in superconducting characteristics affecting the behavior of  $R_s(H_0)$ . One of such key characteristics is the local DOS at the surface, which can be directly probed by tunneling experiments. For instance, calculations of microwave suppression of  $R_s(H_0)$  using the kinetic Usadel equations for dirty superconductors [35,41,44,45] suggest that the  $N$  doping of a few- $\mu\text{m}$ -thick surface layer can result in the field-induced reduction of  $R_s(H_0)$  in two different ways: (1)  $N$  doping mostly reduces the DOS

peaks' broadening in the entire layer of rf-field penetration  $\simeq 2\lambda \sim 100$  nm, which brings about the microwave reduction of  $R_s(H_0)$  characteristic of the idealized BCS model [35,40,41]. (2) The key effect of the  $N$  doping is in modifying the surface-oxide structure, and partial or complete conversion of the metallic suboxides into dielectric (Nb<sub>2</sub>O<sub>5</sub>) or semiconductor (NbO<sub>2</sub>) forms, which do not cause significant rf losses and DOS broadening. In this case, the effect of the  $N$  doping in the bulk mostly manifests itself in the reduction of the mean free path without much effect on the DOS broadening. The effect of a thin proximity-coupled normal layer on the field-induced reduction of  $R_s(H_0)$  was recently calculated in Ref. [45]. The purpose of the present work is to identify the material modifications caused by the  $N$  doping using combined scanning tunneling microscopy (STM) and spectroscopy (STS), and x-ray photoelectron spectroscopy (XPS) to probe the electronic and chemical states of Nb both in the bulk and at the surface.

We perform tunneling spectroscopy and XPS of typically prepared Nb and  $N$ -doped Nb cutouts from SRF cavities. The main goal is to reveal the changes produced by the  $N$  doping in the native oxide and the bulk DOS of typically prepared Nb and understand how these changes manifest themselves in the tunneling spectra in terms of superconducting gap, DOS broadening, and subgap states. Recent work on point-contact tunneling spectroscopy of  $N$ -doped Nb samples [53] addressed the same issues but our work pursues a different approach. We first study native surfaces of Nb and  $N$ -doped SRF cavities cutouts to get insights into the native oxide. Then we perform scanning tunneling microscopy and spectroscopy on the Ar-ion sputtered surfaces of Nb and  $N$ -doped SRF cutouts to infer the bulk DOS underneath the native oxide. This combined approach allows us to discriminate the effect of  $N$  doping on the oxide surface and the bulk DOS. Furthermore, since the sputtered surfaces are metallic it is possible to use the full capability of the scanning tunneling microscope to obtain much larger statistics of tunneling spectra, information about spatial distribution of superconducting properties on submicron scale, and vortex imaging. Scanning tunneling measurements of vortices can directly probe the coherence length by measuring the vortex core size for typically prepared and  $N$ -doped samples. Furthermore, since tunneling spectra also contain information about metallic suboxide overlayers, fitting the observed spectra with a proximity effect theory [44] gives insight into the change of thickness of this layer and the contact resistance between the superconductor and the metallic suboxide layer after the  $N$  doping. These parameters can significantly affect the microwave reduction of the surface resistance [44,45]. Although the Ar-ion sputtering is known to affect the oxide layer and those findings cannot be directly related to the rf performance of cavities, a better understanding of the physics and the materials science that emerges from this

study can indicate important mechanisms by which the performance of Nb resonant cavities can be improved by the materials treatments.

The paper is organized as follows. In Sec. II we describe the experimental setup and procedures as well as typically prepared Nb and nitrogen-doped Nb samples that are investigated. In Sec. III the results of XPS measurements are presented. Section IV contains the results of tunneling spectroscopy measurements. In Sec. V we present STM imaging of vortices. In Sec. VI we discuss the totality of our experimental data and their implications on the effects of  $N$  doping on the electrodynamics of superconducting Nb, with the conclusions summarized in Sec. VII.

## II. EXPERIMENTAL DETAILS

The samples studied in this work [ $5(l) \times 5(w) \times 3(t)$  mm<sup>3</sup>] are cut out from typically prepared Nb and  $N$ -doped superconducting rf cavities. The typically prepared Nb samples are cut from a single-cell 1.3-GHz cavity, labeled  $A2$ , made with ingot niobium from Companhia Brasileira de Metalurgia e Mineração (CBMM). The cavity shape is that of the center cell of TESLA and XFEL cavities [54]. The residual resistivity ratio (RRR) of the niobium is around 260 and the cavity is processed through standard buffered chemical polishing (BCP) to remove approximately 24  $\mu\text{m}$  from the inner surface followed by high-pressure rinsing prior to testing. At 2 K, the cavity reached the quality factor,  $Q_0$ , of around  $6 \times 10^9$  at its peak magnetic field,  $B_p$  of 120 mT. The  $N$ -doped Nb samples are cut from a single-cell 1.3-GHz  $N$ -doped cavity, with the same shape as  $A2$ , labeled TD4. The cavity is fabricated from ingot niobium from Tokyo Denkai with RRR of around 300 with a large grain size of few  $\text{cm}^2$ . Prior to  $N$  doping, the cavity has gone through standard BCP and high-pressure rinsing with ultra-pure water. The nitrogen-doping process for this cavity involved heat treatment at 800 °C and exposure to nitrogen at a pressure of

around 25 mTorr for 20 min. After the nitrogen is removed, the cavity is heated again at 800 °C for 30 min. Finally, approximately 10  $\mu\text{m}$  of the inner surface of the cavity is removed by electropolishing. At 2 K, this cavity achieved a quality factor of  $4 \times 10^{10}$  at its peak magnetic field of 88 mT. Figure 1(a) shows a plot of  $Q_0(B_p)$  for the BCP-treated cavity  $A2$  and  $N$ -doped cavity TD4 measured at 2 and 1.6 K. A thermometry system [55] allows measuring the temperature of the cavities' outer surface with increasing rf field. Figures 1(b) and 1(c) show temperature maps at the highest rf field in cavities  $A2$  and TD4, respectively. The location where “cold spot” samples are cut is shown by a white rectangle in the maps.

All the samples are cut using a CNC milling machine with no lubricant. During the cutting process, the steady flow of compressed helium is applied at the drilling region in order to prevent the sample from heating. The temperature is monitored throughout the process to make sure it did not raise above 32 °C. To verify this cutting process, a TOF SIMS analysis is done on a  $16 \times 16$  mm<sup>2</sup> niobium sample, and the measurements are repeated near the same location after cutting out an  $8 \times 8$  cm<sup>2</sup> sample. The analysis showed some increase in carbon concentration but did not show any new impurities after cutting.

Only cold spots of both types of cavities are measured in order to identify the main differences that improve the performance of the  $N$ -doped Nb cavities. XPS measurements are performed using a PHI Versaprobe 5000 XPS at the Drexel University Core Facilities. The x-ray source used is  $\text{AlK}\alpha$  (1486.6 eV, 200 W). The binding energy is calibrated to the accidental carbon impurity C 1s, C—C bond, at 284.6 eV. The depth profile is performed using Ar-ion sputtering at 1 keV, 2- $\mu\text{A}$  beam current, and  $2 \times 2$  mm<sup>2</sup> beam size. The calibration performed on Nb provided a sputtering rate of 1.1 nm/min. As explained in detail in Sec. III, XPS measurements on native surfaces allow us to get detailed information about the native oxide. Using the depth-profile measurements we then compare

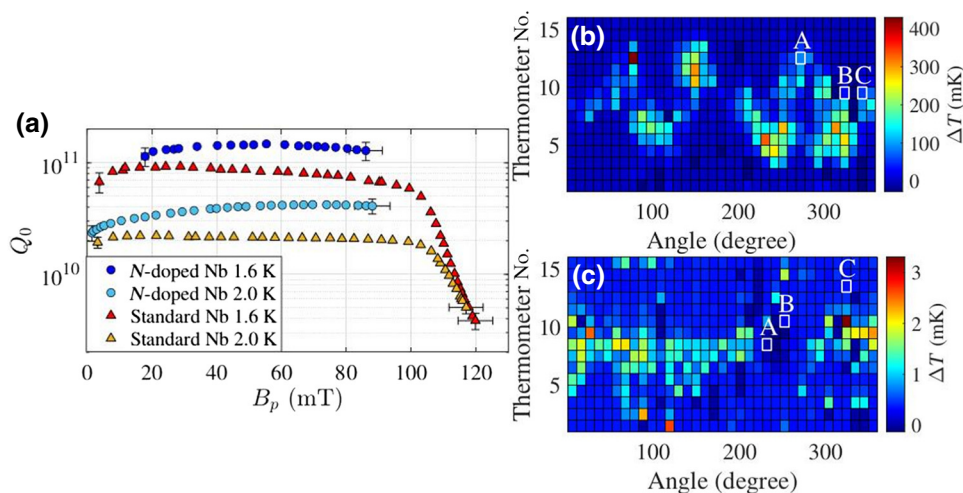


FIG. 1. (a)  $Q_0$  vs  $B_p$  curve for BCP-treated ( $A2$ ) and  $N$ -doped Nb (TD4) cavities at 1.6 and 2.0 K. (b),(c) Temperature maps at 1.6 K on  $A2$  and TD4, respectively, at the highest rf field. The x axis is the azimuthal angle around the cavity, and the thermometer numbers indicate the longitudinal positions with the thermometer N.8 at the equator of the cavity. The cold-spot samples cut out from the locations labeled  $A$  are measured with STM tips breaking the oxide,  $B$  with XPS, and  $C$  with STM after Ar-ion sputtering.



the oxide-layer thickness of the typically prepared Nb and *N*-doped Nb samples. Since Ar sputtering can cause changes in the native oxide, the absolute values of its thickness cannot be readily obtained, yet qualitative conclusions about the effect of *N* doping can still be made.

Low-temperature STM and STS measurements are performed at temperatures ranging from 1.0 to 1.7 K, using a Unisoku ultrahigh vacuum STM system equipped with a 9-T superconducting magnet and with a base pressure of  $4 \times 10^{-11}$  Torr. Pt—Ir tips are used in all measurements. Because the top layer of Nb is dominated by a thick layer of Nb<sub>2</sub>O<sub>5</sub> insulating oxide, it is not possible to tunnel through the native surface. In order to measure the tunneling spectra of the underlying Nb, it is necessary either to break the oxide with the STM tip or to remove the oxide layer by Ar-ion sputtering. Each of these techniques has limitations, but combining them as described below allows us to probe superconducting properties affected by the complex surface-oxide layer in the first few nanometers at the surface of Nb and to trace the effect of *N* doping on the density of states.

For the tunneling measurements performed on native Nb surfaces the tip is used to break the oxide by pushing the tip into the oxide layer until a high current is detected. Typically, this current saturates the preamplifier. After this operation is repeated several times the tip is retracted and using the feedback loop a current of the order of 100 pA is stabilized with a bias of 10 mV and tunneling spectra are acquired. This is repeated at different locations on the sample's surface at a typical distance of several microns away from each other. Furthermore, several measurements are performed on similar samples with different tips to obtain more data statistics. This procedure allows us to get some statistics of spectra but poor correlation between topography and spectra, as the scanning capability of the STM cannot be used at all. Our approach yields information about the electronic structure of a native oxide that acts as a tunnel barrier and proximity layer. When the STM tip is crashing into the complex oxide surface, the tunnel barrier is provided by the oxide itself. In this case tunneling to the bulk superconductor occurs through both a nonuniform normal layer and the sides of the tip. Complex contributions to the tunneling spectrum coming from variable thicknesses of the normal layer and side tunneling from the tip are not well understood and have not yet been taken into account by the existing theoretical models. As discussed in detail in Secs. IV B and VI the limitation of this technique lies in the low statistics and low amount of data that can be adequately fitted and lack of spatial information.

Cleaning the Nb surface with Ar-ion sputtering is done *in situ* soon before transferring the sample to the STM scanner. The sputtering is performed in a preparation chamber attached to the STM with a base pressure of low  $10^{-11}$  Torr. The Ar (purity: 99.999%) partial pressure of

$10^{-5}$  Torr with an energy  $E = 1$  keV for 1 h are the conditions used for all samples. Our estimated removal rate is 0.27 nm/min. This guarantees removal of the known insulating oxide layer from the Nb surface and yields a metallic surface that can be studied by STM, using the full capability of STM and allowing therefore a correlation between topography and spectroscopy. Ar sputtering is known to change the Nb native oxide, but it is not expected to affect the bulk materials properties. Indeed, our simulations of the Ar distribution in Nb using SRIM software [56] have shown that typical penetration depths for 1-KeV Ar ions are about 1–3 nm. Therefore, this method allows us to access the bulk quasiparticle density of states in Nb through a thin layer of metallic oxide and obtain more statistically meaningful data that can be fitted by a proximity effect model, as described in Sec. IV B.

Maps of tunneling spectra are acquired at different locations at a distance of approximately 500  $\mu\text{m}$  from each other to probe regions far away and collect more statistics. Typical maximum scan areas of the order of about 800 nm  $\times$  800 nm allow mapping also inhomogeneities on submicron length scales. Furthermore, when using this sample preparation procedure in the presence of an applied magnetic field perpendicular to the sample surface, vortices are imaged by acquiring conductance maps at the Fermi energy. The conductance maps are acquired by scanning the tip over the sample surface at an energy higher than the superconducting gap (10 mV), acquiring the lock-in signal at the Fermi energy at each location. Conductance maps reveal therefore, vortices by tracking the difference of the electronic density of states inside and outside the vortex cores. Topography is always acquired simultaneously to check the location where the spectroscopic information is recorded. All differential conductance spectra  $dI/dV$  are taken with the same tunneling parameters, with the junction stabilized at  $V = 10$  mV,  $I = 60$  pA, or 100 pA.

### III. X-RAY PHOTOELECTRON SPECTROSCOPY

It is well known that niobium is very reactive to oxygen, and the surface oxidation of niobium has been extensively investigated. The initial stages of oxidation of niobium have been characterized through many studies using XPS [57–61], ultraviolet photoemission [62], Auger electron spectroscopy [63,64], and high-resolution electron-energy-loss spectroscopy [64]. It has been observed that NbO and NbO<sub>2</sub> are initially formed on niobium as a protective layer, with Nb<sub>2</sub>O<sub>5</sub> being formed after further oxidation [57–59,62,64]. Furthermore, Nb<sub>2</sub>O<sub>5</sub> is reduced to NbO<sub>2</sub> and NbO by annealing in ultrahigh vacuum at elevated temperatures above 600 K due to the dissolution of oxygen into the bulk metal [59].

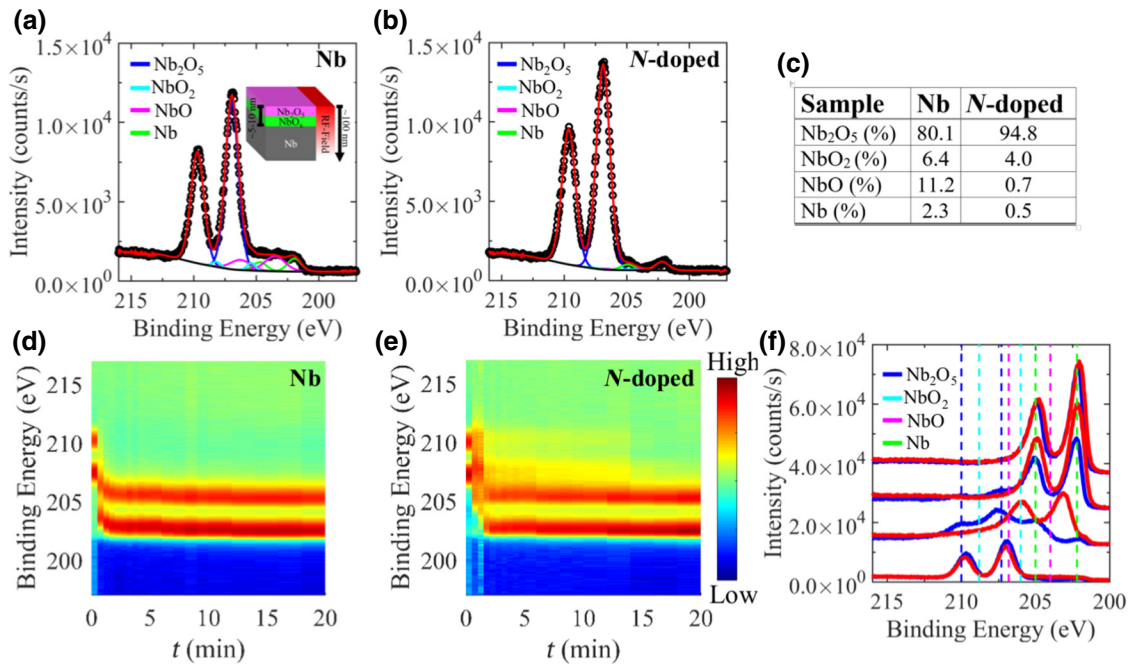


FIG. 2. Nb  $3d$  spectral line together with the deconvolution spectra for different oxidation states for native typically prepared Nb (a) and  $N$ -doped Nb (b). (c) Table shows the spectra deconvolution fitting results for both native surfaces. The native surface of the  $N$ -doped sample shows a significantly more oxidized state with a smaller contribution from the metallic NbO peak. The inset of (a) shows a simplified depiction of the surface-oxide layers of the Nb surface. (d),(e) Color maps of the XPS depth profile obtained while Ar-ion sputtering typically prepared and  $N$ -doped Nb surfaces, respectively. The depth profile shows that the  $N$ -doped sample retains a higher oxidation state, Nb<sub>2</sub>O<sub>5</sub> in particular, as a function of depth. The map is in logarithmic scale to emphasize the retention of higher oxides at the surface. (f) XPS spectra taken at 0, 30, 600, and 1200 s have been offset for clarity. The peaks of the Nb  $3d_{3/2}$  and  $3d_{5/2}$  are shown with vertical lines. Ar-ion sputtering is performed at normal incidence. The electron takeoff angle is  $30^\circ$ .

While it is known that the oxidation states of metals determined by XPS can be in part changed by ion bombardment [65], a qualitative comparison between typically prepared Nb and  $N$ -doped Nb surfaces can still be made. The Nb  $3d$  core level of the native surface of the typically prepared and  $N$ -doped samples can be found in Figs. 2(a) and 2(b), respectively, together with the spectra deconvolution. The Nb  $3d$  peaks from Ref. [59] can be summarized as follows: Nb<sup>5+</sup> (Nb<sub>2</sub>O<sub>5</sub>) peaks are located at 210.0 and 207.3 eV, Nb<sup>4+</sup> (NbO<sub>2</sub>) peaks are located at 208.8 eV and 206.0 eV, Nb<sup>+2</sup> (NbO) peaks are located at 206.8 and 204 eV and Nb<sup>0</sup> peaks are at 205.0 and 202.2 eV. The table summarizing the results of the XPS spectra deconvolution is reported in Fig. 2(c). The surface of both natively oxidized surfaces is dominated by Nb<sub>2</sub>O<sub>5</sub>, as expected. It should be outlined that it is difficult to distinguish stoichiometric Nb<sub>2</sub>O<sub>5</sub> from nonstoichiometric Nb<sub>2</sub>O<sub>5-x</sub> compounds with XPS [66], since the predominant oxidation state is +5 in all compounds. In general, numerous oxygen vacancies exist in Nb<sub>2</sub>O<sub>5</sub> [43,57,67]. Therefore, the large Nb<sub>2</sub>O<sub>5</sub> peaks suggest that a combination of Nb<sub>2</sub>O<sub>5</sub>, nonstoichiometric and locally oxygen-deficient Nb<sub>2</sub>O<sub>5</sub> are present in the samples. The comparison between the two types of surfaces shows a clear difference in the NbO peak

for the two surfaces where the  $N$ -doped sample hardly shows any contribution [Figs. 2(b) and 2(c)].

The XPS spectra obtained while sputtering the typically prepared and  $N$ -doped Nb surfaces with 1 keV Ar ions [Figs. 2(d)–2(f)] show that the sputtering process shifts spectral weight from Nb<sub>2</sub>O<sub>5</sub> to lower Nb oxidation states. Ar-ion sputtering of oxidized Nb is believed to both preferentially remove oxygen from Nb<sub>2</sub>O<sub>5</sub> and diffuse oxygen into bulk Nb [68], thickening the lower oxidation state layers [presented schematically in the inset of Fig. 2(a)]. Despite this, notably the  $N$ -doped Nb surface, while showing the same qualitative behavior as a conventionally prepared Nb surface, appears different as the higher oxidation state seems to be thicker compared to the typically prepared Nb surfaces as shown in the depth profile in Fig. 2(e) and the NbO peak is always lower than that of typically prepared Nb. The same panel also shows that the Nb peaks at 205.0 and 202.2 eV are deeper below the surface compared to the typically prepared Nb surfaces. Even though Ar sputtered surfaces might be partially modified compared to the native surfaces these results unambiguously show that for  $N$ -doped surfaces the higher oxidation states layer of Nb is thicker and that the NbO layer is thinner.

#### IV. TUNNELING SPECTROSCOPY RESULTS

A schematic of our tunneling measurements is shown in Fig. 3. The STM data are analyzed using the standard expression for the tunneling current that flows between a metallic tip and a sample [69]:

$$I = \frac{4\pi e}{\hbar} \int_{-\infty}^{\infty} [f(\epsilon) - f(\epsilon + eV)] N_S(\epsilon) N_T(\epsilon + eV) \times |M(\epsilon)|^2 d\epsilon, \quad (1)$$

where  $f(\epsilon)$  is the Fermi distribution function,  $N_S(\epsilon)$  and  $N_T(\epsilon)$  are the density of states of the sample and tip, respectively,  $V$  is the applied voltage between the tip and the sample and  $M(\epsilon)$  is the tunneling matrix element as a function of the quasiparticle energy  $\epsilon$ . At low temperature  $T \ll \Delta$ , Eq. (1) can be simplified if the applied voltage is much lower than the tunneling energy barrier. If the metallic tip [such as platinum iridium (PtIr)] has a nearly constant density of states in the energy region of interest,  $\epsilon \sim \Delta$  at the Fermi surface,  $N_T(\epsilon)$  in Eq. (1) can be taken out of the integral. In this case the tunneling differential conductance takes the form

$$\frac{dI}{dV} \propto - \int_{-\infty}^{\infty} \frac{\partial f(\epsilon + eV)}{\partial V} N_S(\epsilon) |M(\epsilon)|^2 d\epsilon. \quad (2)$$

The density of states in a superconductor with an ideal surface can be approximated by the widely used phenomenological Dynes formula [69,70]

$$N_S(\epsilon) = N_s \text{Re} \frac{\epsilon + i\Gamma}{\sqrt{(\epsilon + i\Gamma)^2 - \Delta^2}}. \quad (3)$$

Here  $N_s$  is the DOS at the Fermi surface in the normal state, and the parameter  $\Gamma$  quantifies a finite quasiparticle lifetime approximately  $\hbar/\Gamma$  resulting in the broadening

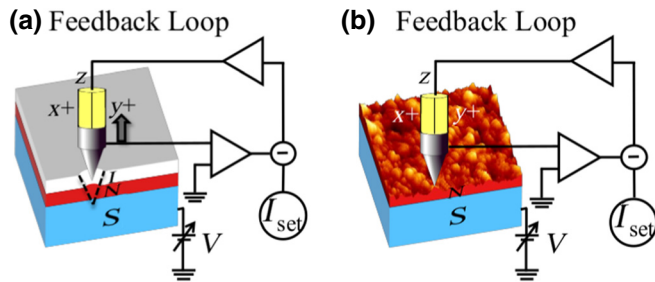


FIG. 3. Schematics of the tunneling measurements performed on (a) native surfaces by crashing the tip into the surface, (b) on Ar-ion sputtered metallic surfaces. The surfaces are metallic after Ar-ion cleaning and this allows operation in the typical scanning modality of the STM. The top image of the sketch is a real representative STM topography image acquired on a Nb surface after Ar-ion sputtering. The scan area is  $156 \times 156 \text{ nm}^2$  and the scanning parameters are  $I_{\text{set}} = 60 \text{ pA}$ ,  $V_{\text{set}} = 100 \text{ mV}$ .

of the gap peaks in the DOS. Different mechanisms can contribute to  $\Gamma$  (see, e.g., Ref. [44]) but irrespective of microscopic details, this broadening and the resulting sub-gap quasiparticle states at  $|\epsilon| < \Delta$  can produce a nonexponential temperature dependence of the surface resistance  $R_s(T)$  at  $T \ll T_c$  and contribute to the residual resistance [41,44,45]. Electron tunneling is a surface-sensitive technique, which directly probes the quasiparticle density of states with high-spatial and high-energy resolution. This makes it a very powerful instrument to investigate the mechanisms that contribute most to the surface resistance of SRF cavities.

A more realistic model that accounts for weakened superconductivity or a thin normal layer at the superconductor surface was recently developed [44,45] based on the Usadel equations [11] for a proximity-coupled dirty normal layer ( $N$ ) on a surface of a bulk superconductor ( $S$ ). In particular, this theory describes a thin metallic suboxide layer at the Nb surface. The position-dependent quasiparticle density of states  $N_N(\epsilon, x)$  across a thin normal layer coupled to the bulk superconductor is determined by a set of equations given in the Appendix. These equations are used to fit our tunneling spectra acquired on Ar-ion sputtered surfaces. The behavior of  $N_N(\epsilon, x)$  is mostly controlled by two dimensionless parameters  $\alpha$  and  $\beta$ , which quantify the effect of the  $N$ -layer thickness and the  $N$ - $S$  interface transparency, respectively:

$$\alpha = \frac{dN_n}{\xi_s N_s}, \quad \beta = \frac{4e^2}{\hbar} R_B N_n \Delta d. \quad (4)$$

Here  $d$  is the thickness of the  $N$  layer,  $\xi_s = (D_s/2\Delta)^{1/2}$  is the coherence length in the bulk superconductor,  $D_s$  is the electron diffusivity,  $N_s$  and  $N_n$  are the DOS at the Fermi surface in the normal state, the subscripts  $n$  and  $s$  corresponds to the parameters of the  $N$  layer and the  $S$  substrate, respectively, and  $R_B$  is a contact resistance of the  $N$ - $S$  interface.

#### A. Native Nb surfaces

Tunneling measurements are performed on the Nb surfaces to get an insight into the native oxide layers of both typically prepared and  $N$ -doped Nb. The oxide layers are too thick [see Fig. 2(b)] to allow direct tunneling into the Nb. Therefore, the STM tip is used to locally break the oxide and by using the feedback loop the tip is then retracted until a stable junction is obtained. Several such junctions are investigated at different locations separated by several microns. At each location 20–50 spectra are acquired and averaged to improve the signal-to-noise ratio.

To analyze the tunneling spectra we first use Eq. (3) of the Dynes model to get a qualitative understanding of the gap distribution as well as the typical values of the DOS broadening parameter  $\Gamma$ . In Figs. 4(a) and 4(b) typical tunneling spectra recorded on typically prepared Nb



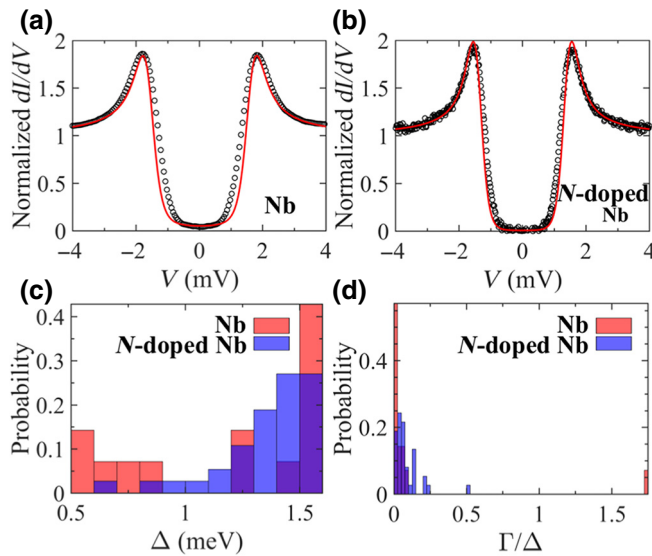


FIG. 4. (a),(b) Typical tunneling spectrum (dots) and BCS-Dynes fit (red line) acquired on Nb and  $N$ -doped Nb, respectively, at  $T = 1.5$  K. The fitting parameters in (a) are  $\Delta = 1.60$  meV and  $\Gamma = 0.08$  meV. The fitting parameters in (b) are  $\Delta = 1.39$  meV and  $\Gamma = 0.01$  meV. (c),(d) Histogram comparison of BCS-Dynes fitting parameters  $\Delta$  and  $\Gamma/\Delta$ , respectively. All parameters are extracted by fitting the model described in the text to the tunneling conductance. Spectra have been acquired several  $\mu\text{m}$  away from each other. For all spectra the tunnel junction is stabilized at  $I_{\text{set}} = 100$  pA and  $V_{\text{set}} = 10$  mV, conductance spectra are acquired with  $V_{\text{mod}} = 200$   $\mu\text{V}$  and  $f = 373.1$  Hz.

and  $N$ -doped Nb are presented together with the fits to Eq. (3) and the resulting fitting parameters. The so-obtained gap values and the ratio  $\Gamma/\Delta$  are summarized in Figs. 4(c) and 4(d). The distribution of the  $\Delta$  values indicate that the average value of  $\Delta$  is higher for typically prepared Nb but also that there is a larger distribution of  $\Delta$  and a higher value of  $\Gamma/\Delta$ , indicating stronger inhomogeneities of superconducting properties in the typically prepared Nb surface layers. The background of the tunneling spectra at higher energy ( $eV > \Delta$ ) exhibits a more parabolic behavior in spectra acquired on typically prepared Nb. A parabolic background is usually related to lower average work function between tip and sample as already reported in other tunneling experiments [53,71]. This difference between the two surfaces appears to be significant and it provides further evidence that the surface is more oxidized in the case of  $N$ -doped Nb, consistent with the data gathered from XPS. This is also in agreement with the earlier results of Ref. [53]. We note that only about 50% of the tunneling spectra acquired on typically prepared Nb surfaces and 70% of the  $N$ -doped Nb tunneling spectra could be properly fitted. Those spectra that could not be properly fitted include gapless spectra obtained more frequently on typically prepared Nb surfaces while about 10% of

the spectra for both surfaces present subgap quasiparticle states or zero conductance peaks.

## B. Scanning tunneling spectroscopy

Ar-ion sputter cleaning of the surface is used to remove the insulating  $\text{Nb}_2\text{O}_5$  layer *in situ*. As mentioned above, Ar sputtering may modify the oxide layer by thickening the metallic suboxide layer. Therefore, the surface layer after Ar sputtering may not be fully representative of the native surface of the cavities. Yet, since the penetration depth of Ar ions at 1 keV is only a few nm [56], this method does not affect the bulk properties and allows us to access directly the DOS of the underlying bulk superconductor that significantly contributes to the cavity rf performance. Moreover, this technique allows us to separate the effect of  $N$  doping on the bulk from that of the oxide layer. Such a surface-cleaning procedure yields metallic surfaces where the full potential of scanning capability of STM and STS can be used and a correlation between topography and spectroscopy be investigated. Calibration of the removal rate is obtained using atomic force microscopy. The removed thickness is estimated to be about 15 nm. A schematic of how the measurements are performed is shown in Fig. 3(b). The sample studied consists of the bulk superconducting and a metallic overlayer. The top image of the schematics is a typical STM topography acquired on an Ar-ion sputtered Nb sample. The roughness of the surface is due in part to the sputtering process and it is of the order of several nm over a scan area of  $800 \times 800$   $\text{nm}^2$ . Tunneling conductance spectra are acquired on the sample surface with a spacing of 32.6 nm in  $390 \times 390$   $\text{nm}^2$  or  $780 \times 780$   $\text{nm}^2$  scan areas. Several spectroscopy grids are acquired on scan areas separated by a typical distance of 500  $\mu\text{m}$ . The spectra are fit using the proximity model [44] with the equations presented in the Appendix. The results of the fitting are summarized in Fig. 5. Figures 5(a) and 5(b) show typical tunneling spectra acquired on typically prepared Nb and  $N$ -doped Nb together with the fitting curve and the fitting parameters. The histograms of the gap values and the broadening parameter  $\Gamma/\Delta_0$  are reported in Figs. 5(c) and 5(d). The average value of  $\Delta_0$  is reduced in the  $N$ -doped Nb samples, but its distribution is narrower than that obtained for the typically prepared Nb surfaces. The values of the Dynes broadening parameter  $\Gamma$  are larger for the typically prepared Nb surfaces. The broadening of the gap peaks in the quasiparticle density of states  $N(\epsilon)$  in the bulk gives rise to a weakly temperature-dependent residual surface resistance [44].

The fits show that the parameter  $\alpha$  [Fig. 5(e)], proportional to the thickness of the normal suboxide layer, is in average larger for the typically prepared Nb. The parameter  $\beta$  [Fig. 5(f)], proportional to the contact resistance between the superconductor and the normal layer, is more distributed for the typically prepared Nb. Interestingly, the

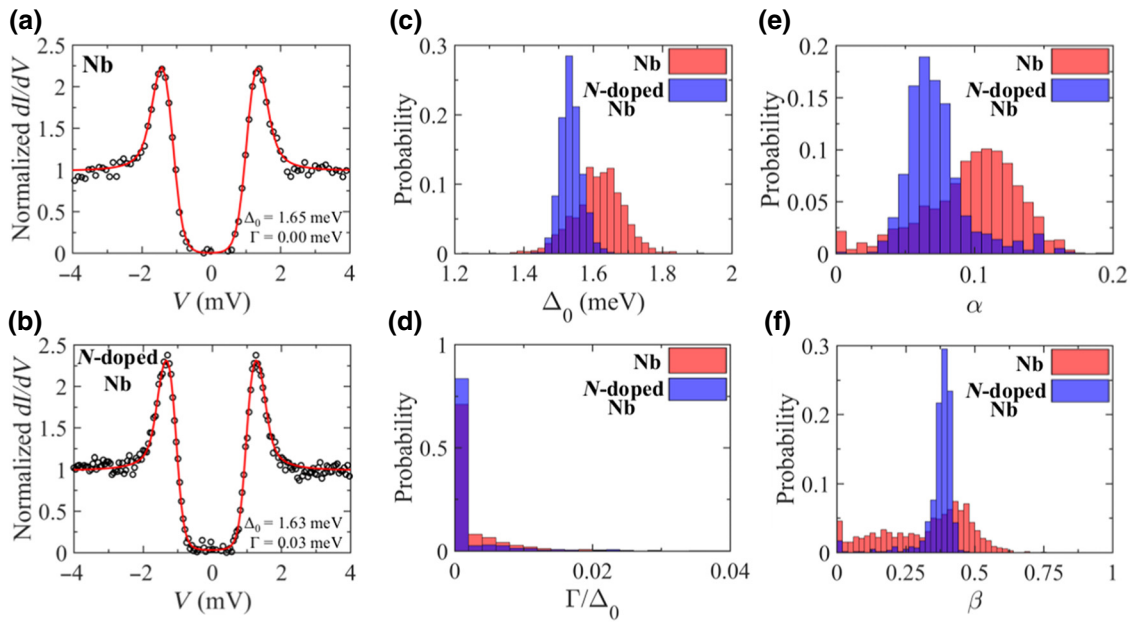


FIG. 5. (a),(b) Typical tunneling spectra (dots) acquired on typically prepared Nb and *N*-doped Nb surfaces. The red lines are the fit obtained using the model of Ref. [44] described in the text and equations presented in the Appendix. (c),(d) Histogram comparison of the fit parameters  $\Delta_0$  and  $\Gamma/\Delta_0$ , respectively. (e),(f) Histogram comparison of the fit parameters  $\alpha$  and  $\beta$ , respectively. For typically prepared samples the number of spectra analyzed is  $N = 1440$  (red) and for *N*-doped samples  $N = 576$  (blue). Spectra are taken 32.6 nm away from each other, at  $T = 1.5$  K with  $I_{\text{set}} = 60$  pA,  $V_{\text{set}} = 10$  mV with a lock-in modulation  $V_{\text{mod}} = 200$   $\mu\text{V}$  and  $f = 373.1$  Hz.

fit values of  $\beta$  cluster around  $\beta \simeq 0.3$ – $0.4$  for the *N*-doped samples. As follows from the calculations of Ref. [44], low values of  $\Gamma$  together with  $\beta$  ranging between 0.3 and 0.4, can significantly reduce the surface resistance. This is due to the long-range disturbance in the density of states produced by the *N* layer into the superconductor, which outweighs the contribution of the subgap states in the proximity coupled normal layer. Finally, in the case of sputtered surfaces we find that the tunneling spectra of typically prepared Nb present a nonlinear background that indicates a lower tunnel barrier than for *N*-doped Nb, in agreement with the results previously observed in Ref. [53].

Figure 6 shows the spatial variation of some of the fitting parameters on a typical scan area of  $780 \times 780$  nm<sup>2</sup>. The comparison between the typically prepared Nb and the *N*-doped Nb in Figs. 6(a) and 6(b) shows that for typically prepared Nb there are variation of  $\Delta_0$  and  $\beta$  on a submicron scale. More uniform values for the *N*-doped Nb are instead obtained.

## V. VORTICES

If a magnetic field is applied, Abrikosov vortices can penetrate into the sample and modify the local density of states. Hot spots resulting from vortex bundles trapped during the cavity cooldown through  $T_c$  can not only limit the performance of SRF cavities [13–20] but also contribute to the field-induced decrease of  $R_s(H_0)$  [52]. Imaging of

vortices can give valuable information about the electronic structure of the vortex core in the first few nm at the surface, which plays the key role in rf dissipation. Vortices can

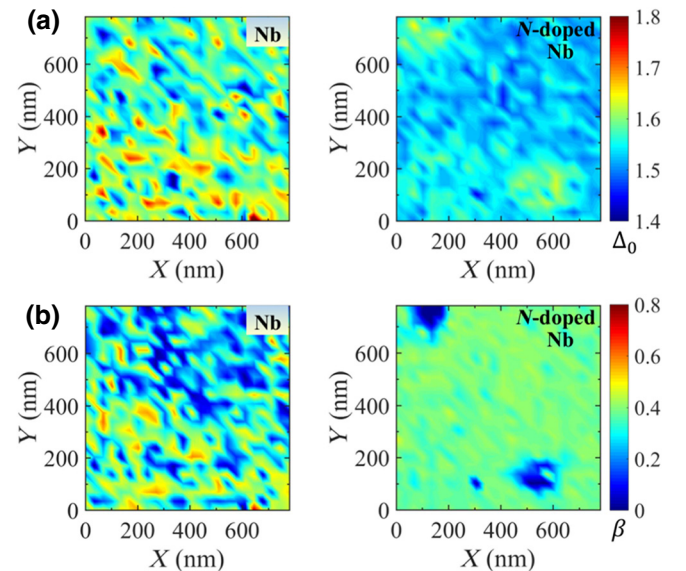


FIG. 6. Local maps of  $\Delta_0$  (a) and  $\beta$  (b) over  $24 \times 24$  pixels. The parameters are extracted by fitting the tunneling spectra acquired at each location with the proximity model [44] described in the text. Spectra are taken 32.6 nm away from each other at the tunneling parameters of  $I_{\text{set}} = 60$  pA,  $V_{\text{set}} = 10$  mV,  $V_{\text{mod}} = 200$   $\mu\text{V}$ ,  $f = 373.1$  Hz, and  $T = 1.0$ – $1.7$  K.

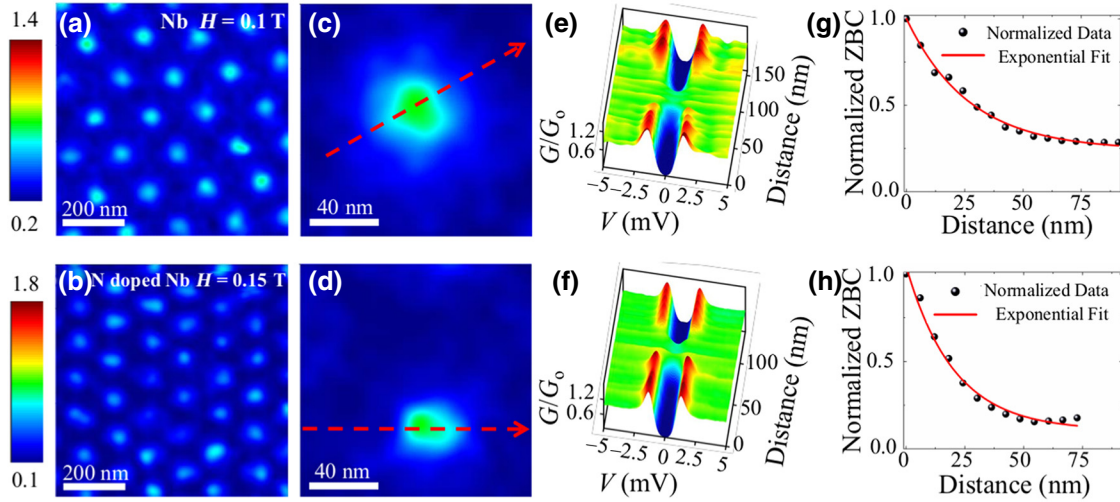


FIG. 7. Tunneling conductance-map images acquired at the Fermi level  $E_F$  showing the vortex lattice at  $T = 1.5$  K on a typically prepared Nb surface (a) and on a  $N$ -doped Nb surface (b). The images are acquired in magnetic fields of 100 mT (a) and 150 mT (b) applied perpendicular to the surface. The scan area is  $745 \times 745$  nm<sup>2</sup> for both images. (c),(d) High-resolution single-vortex image at the same temperature and same field for Nb (c) and  $N$ -doped Nb (d). The scan area is  $134 \times 134$  nm<sup>2</sup>. (e),(f) A series of 100 tunneling spectra ( $dI/dV$ ) acquired along the red dashed lines shown in (c) and (d). In all images and line spectra the tip is stabilized at  $V = 10$  mV and  $I = 60$  pA and a lock-in bias modulation amplitude  $V_{\text{mod}} = 0.2$  mV is used. (g),(h) Evolution of normalized zero bias conductance (ZBC) as a function of position from the vortex core. The ZBC is extracted for each vortex in images (a) and (b) except those close to the edges, the average is then normalized by the ZBC value at the vortex core.

be imaged by STM by mapping the local conductance at an energy where a vortex alters the density of states. Therefore, STM is a direct experimental technique to visualize vortices in superconductors with a subnanometer spatial resolution.

Figures 7(a) and 7(b) show the vortex lattice imaged on typically prepared Nb and  $N$ -doped Nb. A triangular vortex lattice has been observed for both types of samples with their intervortex spacing in agreement with the theoretical predictions [48,72,73]. High-resolution single-vortex images are shown in Figs. 7(c) and 7(d). A series of 100 tunneling spectra is acquired across the vortex core for the two samples [Figs. 7(e) and 7(f)]. The line spectra show the spatial evolution of the tunneling spectra with the coherence peak vanishing at the vortex core on a length scale given by the coherence length. In the clean limit, in conventional BCS-like superconductors the tunneling spectra at the vortex center reveal the presence of a peak at zero energy (Fermi level), which is a signature of low-lying Caroli-de Gennes-Matricorn bound states [74] localized in the vortex core [75]. These states are similar to ballistic Andreev trajectories in short superconductor–normal-superconductor junctions. However, in dirty superconductors, where the superconducting coherence length  $\xi \simeq (l\xi_0)^{1/2}$  is larger than the mean free path  $l$  the core levels are broadened by impurity scattering, resulting in a flat DOS in the vortex core [76]. The absence of discrete vortex core levels suggests that both samples are in a moderately dirty limit. The vortex shape seems to be dependent on the

surface roughness, which is about several nm over the lateral scale of  $\simeq 800$  nm. The coherence length is estimated using several methods, which yield similar results.

In Figs. 7(g) and 7(h) the coherence length  $\xi$  is evaluated by azimuthally averaging the zero bias conductance around vortex centers on the conductance maps. The azimuthally averaged tunneling conductance, for all the vortices in the maps neglecting the ones on edges, is then fitted to an exponential function of the form  $g = g_0 + F \exp(-r/\xi)$ , where  $g_0$  is the conductance far from the vortex core,  $F$  is a scaling factor, and  $r$  is the distance from the vortex core. For the typically prepared Nb we obtain a coherence length of  $\xi \approx 26.9 \pm 1.8$  nm smaller than  $\xi_0 \approx 38$  nm for a clean Nb. This suggests that the surface of the untreated Nb sample is in a moderately dirty limit. For the  $N$ -doped Nb, we obtain a yet shorter coherence length  $\xi \approx 20.4 \pm 1.9$  nm. This result clearly shows that the nitrogen doping results in additional impurity scattering, which reduced the mean free path and the coherence length at the surface. Using these values of  $\xi$  in the Ginzburg-Landau expression [72,73] for the upper critical field  $B_{c2} = \Phi_0/2\pi\xi^2$ , we find  $B_{c2} = 460$  mT for typically prepared Nb and  $B_{c2} = 790$  mT for  $N$ -doped Nb. These numbers are consistent with the values of the upper critical field measured from the tunneling spectra acquired in applied magnetic field. The tunneling spectra acquired as a function of applied magnetic field, away from vortices, on the typically prepared Nb sample are presented in the inset of Fig. 8. The zero bias conductance (i.e., the density of states at the Fermi energy),



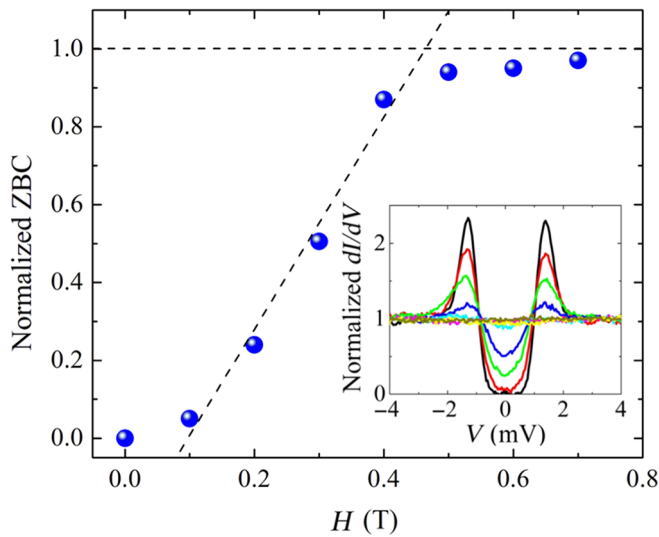


FIG. 8. Normalized zero bias conductance as a function of the applied magnetic field at  $T = 1.5$  K for typically prepared Nb. The estimated upper critical field is approximately 450–500 mT. The inset shows tunneling spectra  $dI/dV$  acquired at 1.5 K at different magnetic fields (from 0 to 0.7 T) applied perpendicular to the sample’s surface. Tunneling conditions are  $V = 10$  mV,  $I = 60$  pA, lock-in modulation  $V_{\text{mod}} = 0.2$  mV and frequency  $f = 373.1$  Hz for all spectra.

acquired at the midpoint between vortices, is shown as a function of field in the main panel of Fig. 8. Here  $B_{c2}$  is estimated as the intersection of the high field slope and the normalized zero-bias-conductance value at  $H > H_{c2}$ .

## VI. DISCUSSION

The top surface of Nb has a complex oxide structure revealed by XPS measurements. Tunneling measurements performed on native surfaces probe mostly the very top layer through a tunnel barrier produced by the native surface oxide. However, Ar sputtering removes the dielectric oxide so the top surface layer becomes metallic and tunneling probes the electronic state of the Nb underneath the suboxide layer through a vacuum barrier.

The tunneling spectra shown in Fig. 4 reveal a large spread of gap values down to very small  $\Delta$  on both typically prepared Nb and  $N$ -doped native surfaces. These very low values of  $\Delta$  are indicative of strong spatial inhomogeneities of superconducting properties that may result from thick metallic suboxide islands. Our results show that nitrogen doping reduces the spread of  $\Delta$  making properties more uniform. This conclusion is consistent with the more uniform distribution of  $\Delta$  observed by first tunneling measurements on titanium-doped Nb cavities exhibiting the extended  $Q(H_0)$  rise [26].

It should be noted that about 50% of the data obtained on native typically prepared Nb surfaces and 30% of the data obtained on  $N$ -doped Nb surfaces cannot be properly

fitted by either the Dynes model or the proximity model [44]. This is hardly surprising given the complexity of the electronic structure of the oxidized surface and its manifestations in superconducting properties. Moreover, the interpretation of experimental data for the STM tip crashing into the complex oxide surface requires proper theoretical analysis of tunneling through the complex oxide of variable thickness and the side tunneling from the tip, which has not been done yet. Nevertheless, our tunneling data and their analysis based on simple models may capture the essential effects of  $N$  doping on the thickness of the normal suboxide layer and the resistive barrier between this layer and the bulk Nb. The fact that some spectra cannot be properly fitted with the existing theoretical models reinforces the need for a better understanding of the rich physics and materials science of the Nb surface. For instance, many spectra appear gapless, possibly indicating the presence of a thick metallic oxide with very small minigap energies of quasiparticles [44]. Some spectra have zero bias peak or deep subgap states, which could indicate the presence of magnetic impurities [43] or perhaps two-level states at the surface [51]. Some spectra exhibit higher energy features characteristic of inelastic tunneling. Some of these features may result from the fact that extracting reliable quantitative information from tunneling spectra obtained on native Nb surfaces by crashing the tunneling tip through the oxide structure is not a very controlled and consistent procedure. Yet, the typically prepared Nb surfaces generally have a parabolic background typical of a lower work function compared to  $N$ -doped surfaces. This indicates that the surface of  $N$ -doped samples are more oxidized, consistent with XPS measurements and earlier point-contact measurements [53].

Our tunneling measurements on Ar-ion sputtered typically prepared Nb and  $N$ -doped Nb cannot give information about the native Nb oxide but allow us to get important information about the bulk superconducting properties and their lateral inhomogeneities underneath the oxide layer. These results can give insights into new ways of boosting the performance of SRF cavities by materials treatments and surface nanostructuring [44,45], even though the information about the oxide layer obtained after ion sputtering cannot be related directly to SRF cavities since the native oxide layer changes upon Ar sputtering.

These measurements reveal clear differences of the Nb underneath the oxide layer for typically prepared and  $N$ -doped Nb, as shown in Fig. 5. Generally, the typically prepared Nb has higher gap and the Dynes broadening parameter  $\Gamma$  as compared to the  $N$ -doped Nb, but also a significantly larger spread of local  $\Delta$  and  $\Gamma$  values. This means that typically prepared Nb has stronger spatial inhomogeneities of superconducting properties, consistent with the above results for native surfaces. Moreover, the fits of the tunneling spectra to the  $N$ - $S$  proximity-coupled model [44] have shown that the nitrogen doping reduces both the

parameter  $\alpha$ , proportional to the thickness of the metallic suboxide layer, and the lateral spread of the local  $\alpha$  values. As follows from Fig. 5(e), the nitrogen doping reduces the peak values of  $\alpha \approx d/\xi_s$  from  $\simeq 0.1$  down to approximately equal to 0.06. Therefore, tunneling measurements suggest that the metal suboxide layer gets thinner after  $N$  doping, in agreement with XPS data. Since Ar sputtering is expected to thicken the metallic suboxide layer, our tunneling data can only be understood if the metallic suboxide layer is thinner in the  $N$ -doped samples of the native surface. While the surface of Ar sputtered samples may not be fully representative of the inner surface of Nb cavities, the Ar sputtering technique can nevertheless give important insights into the effect of  $N$  doping on the nanoscale oxide layer.

The effect of the nitrogen doping on the parameter  $\beta$  proportional to the  $N$ - $S$  contact resistance  $R_B$  is also quite striking. As follows from Fig. 5(f), the nitrogen doping significantly shrinks the wide spread of  $\beta$  and eliminates most of the low- $\beta$  and high- $\beta$  values observed on the typically prepared Nb. Moreover, the nitrogen doping results in a much narrower distribution of local  $\beta$  values clustered at around  $\beta = 0.3$ – $0.4$ , where the  $N$ - $S$  proximity model [44] predicts a minimum in  $R_s$ , which can become smaller than  $R_s$  for an ideal surface. This optimal surface resistance results from a long-range disturbance of the local DOS into the superconductor, which reduces  $R_s$  and outweighs an increase of  $R_s$  due to minigap states in the proximity-coupled normal layer. The elimination of low- $\beta$  values likely comes from the increase in the contact resistance,  $R_B$ , due to the increase in oxidation of the surface corroborated by XPS. Materials mechanisms by which high-temperature treatment during the nitrogen doping affects the contact resistance  $R_B$  are not well understood, but their effect on  $R_B$  can be quite significant. For example, an optimal heat treatment can reduce  $R_B$  between Ag and  $\text{YBa}_2\text{Cu}_3\text{O}_7$  by several orders of magnitude [77,78]. In any case, changing the parameter  $\beta$  towards its optimum value revealed by the results shown in Fig. 5(f) would help push the quality factor towards or beyond its theoretical maximum for a perfect surface. The effect of  $N$  doping on the metallic suboxide layer inferred from the tunneling data of this work can help optimize both the low-field and high-field surface resistance by tuning the DOS by surface nanostructuring, as predicted by recent calculations [44,45].

The values of  $\alpha$  and  $\beta$  cannot be directly related to the native surface of the Nb cavities, as these values have been obtained after Ar sputtering. Yet because both the typically prepared Nb and  $N$ -doped Nb samples are subject to the same Ar sputtering process, which however produce different values for  $\alpha$  and  $\beta$ , it is reasonable to suggest that these differences do result from the  $N$  doping. Thus, our integrated approach that combines such complementary techniques as XPS, and STM and STS coupled to theory

allows us to separate the effect of  $N$  doping in the oxide layer from that in the bulk. This, in turn, can give insights into a rather complex interplay of the materials science and superconductivity at the Nb surface, suggesting new ways of further reducing rf losses of already extremely high- $Q$  niobium resonators.

## VII. CONCLUSIONS

We perform XPS and tunneling measurements on native surfaces and Ar sputtered surfaces of typically prepared and  $N$ -doped Nb cutouts from SRF cavities. The results presented above suggest that the nitrogen doping gives rise to the following effects: (1) slightly reduces the average superconducting gap  $\bar{\Delta}$  while significantly reducing spatial inhomogeneities of  $\Delta$  and the DOS broadening parameter  $\Gamma$  in the bulk, as shown by STM of the Ar-ion sputtered surfaces. (2) Reduces the thickness of the metallic suboxide layer because of its partial conversion into semiconducting or dielectric oxides  $\text{NbO}_2$  and  $\text{Nb}_2\text{O}_5$  as clearly shown by the XPS results and supported by tunneling data on Ar sputtered surfaces. (3) Significantly reduces spatial inhomogeneities of the Nb suboxide thickness and the interface contact resistance parameter  $\beta$  on the Ar sputtered surfaces. Interestingly, the  $\beta$  values for the  $N$ -doped samples become clustered at 0.3–0.4 close to an optimum  $\beta$  that would yield a minimum theoretical low-field surface resistance in the dirty limit [44]. All in all, these effects of the nitrogen doping drastically reduce the material's broadening of the quasiparticle density of states and bring it toward an optimal DOS, which can theoretically minimize  $R_s$ . These experimental results give insight into some possible scenarios by which the nitrogen doping causes the decrease of the surface resistance with the rf field.

The decreases of  $R_s(H_0)$  with the rf field can possibly result from the current-induced broadening of DOS at  $\Gamma \ll T$  and  $\omega \ll T$ , as shown by calculations of  $R_s(H_0)$  from the time-dependent Usadel equations in the dirty limit [35,41,45]. The reduction of  $R_s(H_0)$  due to this mechanism becomes more pronounced at higher frequencies as the effect of the current-induced broadening of DOS on  $R_s(H_0)$  gets amplified by nonequilibrium effects [41]. However, if the native materials broadening of the DOS peaks due to thick suboxide metallic layer and large  $\Gamma$  is strong enough, the current-induced broadening of DOS at high rf fields is not sufficient to turn the conventional decrease of  $R_s(H_0)$  with  $H_0$  into the descending  $R_s(H_0)$ . But if the materials broadening of DOS is ameliorated by the nitrogen doping, as we observe in this work, the current-induced broadening of DOS can take over and  $R_s(H_0)$  starts decreasing with  $H_0$ . In this scenario  $R_s(H_0)$  can be reduced by engineering an optimum DOS at the surface using pairbreaking mechanisms, such as magnetic impurities or surface nanostructuring [44]. Detailed calculations of the interplay of the effects of proximity-coupled



$N$  layer, Dynes parameter, and current-induced broadening of DOS on the field dependence of the nonlinear surface resistance  $R_s(H_0)$  are performed recently in Ref. [45]. Using the theory of Refs. [35,41,44,45], we can infer that the STM results of this work indicate that the decrease of  $R_s(H_0)$  with  $H_0$  caused by the nitrogen doping primarily results from the shrinkage of the metallic suboxide layer rather than the decrease of the parameter  $\Gamma$  in the bulk.

STM imaging of vortices has clearly shown that the nitrogen doping decreases the mean free path  $l$  and the coherence length down to  $\xi \simeq 20$  nm, nearly half of  $\xi_0 \simeq 38$  nm in the clean limit. This suggests that the  $N$ -doped surface is in a moderately dirty limit with the mean free path  $l \sim \xi^2/\xi_0 \simeq 10$  nm. It should be noted that the presence of a proximity-coupled  $N$  layer at the surface increases the diameter of the vortex core at the surface, as shown by recent calculations of  $N$ - $S$  bilayers [79,80]. Yet these calculations show that for a thin  $N$  layer with  $d \ll \xi_s$  characteristic of our Nb surfaces, the effect of the metallic suboxide on the vortex core diameter observed by STM is rather weak so the actual  $\xi_s$  underneath the metallic suboxide is only a bit shorter than the estimates given above. Therefore, tunneling spectroscopy coupled to other surface analysis techniques such as XPS are effective methods to reveal the evolution of the surface DOS due to the materials treatments. This, in turn, can help engineer an optimum DOS by impurity management and surface-oxide nanostructuring to boost the performance of SRF resonant cavities.

## ACKNOWLEDGMENTS

This work is supported by the National Science Foundation, Division of High Energy Physics, under Award No. 1734075. G.C. is supported by Jefferson Science Associates, LLC under U.S. DOE Contract No. DE-AC05-06OR23177. The authors acknowledge the use of the Core Facilities at Drexel University for the X-Ray Photoelectron Spectroscopy (XPS) measurements. Some of the calculations are carried out on Temple University's HPC resources and thus is supported in part by the National Science Foundation through major research instrumentation Grant No. 1625061 and by the US Army Research Laboratory under Contract No. W911NF-16-2-0189.

## APPENDIX: LOCAL DOS IN A PROXIMITY COUPLED $N$ LAYER ON THE $S$ SUBSTRATE

Here we present the formulas obtained in Ref. [44] for the local DOS in a thin  $N$  layer coupled with a bulk superconductor ( $S$ ) by the proximity effect. We use these formulas to fit the STM spectra measured on the typically prepared Nb and nitrogen-doped Nb samples. The local

DOS is given by

$$N_N(\epsilon, x) = N_n \text{Re} \left[ \frac{\cosh \theta_0 - i\beta\tilde{\epsilon}}{\sqrt{1 - \beta^2\tilde{\epsilon}^2 - 2i\beta\tilde{\epsilon} \cosh \theta_0}} - \frac{i\tilde{\epsilon}x(x+2d) \sinh^2 \theta_0}{2\xi_N^2(1 - \beta^2\tilde{\epsilon}^2 - 2i\beta\tilde{\epsilon} \cosh \theta_0)} \right], \quad (\text{A1})$$

$$N_S(\epsilon, x) = N_s \text{Re} \left[ \frac{\tilde{\epsilon}(1 + 6t^2 + t^4) + 4t(1 + t^2)}{(1 - t^2)^2 \sqrt{\tilde{\epsilon}^2 - 1}} \right], \quad (\text{A2})$$

where  $\tilde{\epsilon} = \epsilon + i\Gamma$ ,  $\xi_N = (\hbar D_n/2\Delta)^{1/2}$ , the parameters  $\alpha$  and  $\beta$  are defined by Eq. (4), and  $x$  is the coordinate across the  $N$  layer located at  $-d < x < 0$ . Furthermore,

$$t(x) = \left( \tanh \frac{\theta_0 - \theta_\infty}{4} \right) e^{-k_\epsilon x}. \quad (\text{A3})$$

Here  $k_\epsilon = [\Delta^2 - \tilde{\epsilon}^2]^{1/4} (2/\hbar D_s)^{1/2}$ ,  $\sinh \theta_\infty = \Delta/\sqrt{\tilde{\epsilon}^2 - \Delta^2}$ , and  $\theta_0$  satisfies the following self-consistency equation:

$$2k_\epsilon \sinh \frac{\theta_0 - \theta_\infty}{2} = i\tilde{\epsilon} \Phi \sinh \theta_0 + i\Psi \cosh \theta_0, \quad (\text{A4})$$

which takes into account the proximity effect in the  $N$  layer and a local reduction of  $\Delta(x)$  in the  $S$  region at the  $N$ - $S$  interface. The parameters  $\Phi$  and  $\Psi$  are given by

$$\Phi = \frac{\alpha}{\sqrt{1 - \beta^2\tilde{\epsilon}^2 - 2i\beta\tilde{\epsilon} \cosh \theta_0}}, \quad (\text{A5})$$

$$\Psi = \frac{\alpha(\beta - 1)}{1 + \beta^2} + \frac{\alpha}{(1 + \beta^2)^{3/2}} \ln \frac{(1 + \beta\Lambda)(\beta + \sqrt{1 + \beta^2})}{\sqrt{(1 + \Lambda^2)(1 + \beta^2)} - \Lambda + \beta}, \quad (\text{A6})$$

where  $\Lambda = \hbar\Omega/\Delta$ , and  $\Omega$  is the Debye frequency. For Nb with  $\Delta \simeq 17.5$  K and  $\hbar\Omega/k_B \simeq 275$  K, we have  $\Lambda \simeq 15.7$ . Since the STM spectra are taken at low temperatures  $T \simeq 1$ – $1.5$  K well below  $T_c = 9.2$  K, we use the bulk pair potential  $\Delta$  in the  $S$  region at  $T = 0$ . In the case of weak DOS broadening ( $\Gamma \ll \Delta$ ),  $\Delta$  simplifies to [44]

$$\Delta = \Delta_0 - \Gamma, \quad \Delta_0 = 1.84k_B T_c. \quad (\text{A7})$$

We calculate the local DOS by solving Eqs. (A1)–(A7) numerically using a MATLAB code for different values of the fit parameters  $\alpha$  and  $\beta$ , assuming that  $N_s = N_n$  and  $\Gamma_s = \Gamma_n = \Gamma$ . In the relevant case of  $d \ll \xi_N$ , the local

DOS probed by STM is nearly constant across the thin  $N$  layer, so we calculate  $N_N$  from Eq. (A1) at  $x = 0$ .

- 
- [1] J. Zmuidzinas, Superconducting microresonators: Physics and applications, *Annu. Rev. Condens. Matter Phys.* **3**, 169 (2012).
- [2] M. H. Devoret and R. J. Schoelkopf, Superconducting circuits for quantum information: An outlook, *Science* **339**, 1169 (2013).
- [3] M. A. Hein, in *Microwave Superconductivity*, edited by H. Weinstock, NATO ASI Series E: Applied Sciences Vol. 375 (Kluwer, Dordrecht, 2002), p. 21.
- [4] H. Padamsee, J. Knobloch, and T. Hays, *RF Superconductivity for Accelerators* (Wiley, New York, 2008), 2nd ed., ISBN: 978-3-527-40842-9.
- [5] C. Z. Antoine, *Materials and Surface Aspects in the Development of SRF Niobium Cavities*, EuCARD Editorial Series on Accelerator Science (Warsaw University of Technology, Warsaw, 2012).
- [6] A. Gurevich, Superconducting radio-frequency fundamentals for particle accelerators, *Rev. Accel. Sci. Technol.* **5**, 119 (2012).
- [7] H. S. Padamsee, Superconducting radio-frequency cavities, *Annu. Rev. Nucl. Particle Sci.* **64**, 175 (2014).
- [8] D. C. Mattis and J. Bardeen, Theory of the anomalous skin effect in normal and superconducting metals, *Phys. Rev.* **111**, 412 (1958).
- [9] R. H. Parmenter, Nonlinear electrodynamics of superconductors with a very small coherence distance, *RCA Rev.* **26**, 323 (1962).
- [10] J. Bardeen, Critical fields and currents in superconductors, *Rev. Mod. Phys.* **34**, 667 (1962).
- [11] N. B. Kopnin, *Theory of Nonequilibrium Superconductivity* (Oxford Univ. Press, New York, 2001).
- [12] C. Z. Antoine, Influence of crystalline structure on rf dissipation in superconducting niobium, *Phys. Rev. Accel. Beams* **22**, 034801 (2019).
- [13] A. Gurevich and G. Ciovati, Effect of vortex hotspots on the radio-frequency surface resistance of superconductors, *Phys. Rev. B* **87**, 054502 (2013).
- [14] J.-M. Vogt, O. Kugeler, and J. Knobloch, Impact of cooldown conditions at  $T_c$  on the superconducting rf cavity quality factor, *Phys. Rev. ST Accel. Beams* **16**, 102002 (2013).
- [15] A. Romanenko, A. Grassellino, O. Melnychuk, and D. A. Sergatskov, Dependence of the residual surface resistance of superconducting radio frequency cavities on the cooling dynamics around  $T_c$ , *J. Appl. Phys.* **115**, 184903 (2014).
- [16] M. Martinello, M. Checchin, A. Grassellino, A. C. Crawford, O. Melnychuk, A. Romanenko, and D. A. Sergatskov, Magnetic flux studies in horizontally cooled elliptical superconducting cavities, *J. Appl. Phys.* **118**, 044505 (2015).
- [17] J.-M. Vogt, O. Kugeler, and J. Knobloch, High-Q operation of superconducting rf cavities: Potential impact of thermocurrents on the rf surface resistance, *Phys. Rev. ST Accel. Beams* **18**, 042001 (2015).
- [18] S. Huang, T. Kubo, and R. L. Geng, Dependence of trapped-flux-induced surface resistance of a large-grain Nb superconducting radio-frequency cavity on spatial temperature gradient during cooldown through  $T_c$ , *Phys. Rev. Accel. Beams* **19**, 082001 (2016).
- [19] D. Gonnella, J. Kaufman, and M. Liepe, Impact of nitrogen doping of niobium superconducting cavities on the sensitivity of surface resistance to trapped magnetic flux, *J. Appl. Phys.* **119**, 073904 (2016).
- [20] S. Posen, M. Checchin, A. C. Crawford, A. Grassellino, M. Martinello, O. S. Melnychuk, A. Romanenko, D. A. Sergatskov, and Y. Trenikhina, Efficient expulsion of magnetic flux in superconducting radiofrequency cavities for high  $Q_0$  applications, *J. Appl. Phys.* **119**, 213903 (2016).
- [21] B. Oripov, T. Bieler, G. Ciovati, S. Calatroni, P. Dhakal, T. Junginger, O. B. Malyshev, G. Terenziani, A.-M. Valente-Feliciano, R. Valizadeh, S. Wilde, and S. M. Anlage, High-Frequency Nonlinear Response of Superconducting Cavity-Grade Nb Surfaces, *Phys. Rev. Appl.* **11**, 064030 (2019).
- [22] A. Grassellino, A. Romanenko, D. Sergatskov, O. Melnychuk, Y. Trenikhina, A. Crawford, A. Rowe, M. Wong, T. Khabiboulline, and F. Barkov, Nitrogen and argon doping of niobium for superconducting radio frequency cavities: A pathway to highly efficient accelerating structures, *Supercond. Sci. Technol.* **26**, 102001 (2013).
- [23] A. Romanenko, A. Grassellino, A. C. Crawford, D. A. Sergatskov, and O. Melnychuk, Ultra-high quality factors in superconducting niobium cavities in ambient magnetic fields up to 190 mG, *Appl. Phys. Lett.* **105**, 234103 (2014).
- [24] D. Gonnella, R. Eichhorn, F. Furuta, M. Ge, D. Hall, V. Ho, G. Hoffstaetter, M. Liepe, T. O'Connell, S. Posen, P. Quigley, J. Sears, V. Veshcherevich, A. Grassellino, A. Romanenko, and D. A. Sergatskov, Nitrogen-doped 9-cell cavity performance in a test cryomodule for LCLS-II, *J. Appl. Phys.* **117**, 023908 (2015).
- [25] G. Ciovati, P. Dhakal, and A. Gurevich, Decrease of the surface resistance in superconducting niobium resonator cavities by the microwave field, *Appl. Phys. Lett.* **104**, 092601 (2014).
- [26] P. Dhakal, G. Ciovati, G. R. Myneni, K. E. Gray, N. Groll, P. Maheshwari, D. M. McRae, R. Pike, T. Proslie, F. Stevie, R. P. Walsh, Q. Yang, and J. Zasadzinski, Effect of high temperature heat treatments on the quality factor of a large-grain superconducting radio-frequency niobium cavity, *Phys. Rev. ST Accel. Beams* **16**, 042001 (2013).
- [27] G. Ciovati, P. Dhakal, and G. R. Myneni, Superconducting radio-frequency cavities made from medium and low-purity niobium ingots, *Supercond. Sci. Technol.* **29**, 064002 (2016).
- [28] J. T. Mascalco, D. Gonnella, and M. Liepe, The importance of the electron mean free path for superconducting radio-frequency cavities, *J. Appl. Phys.* **121**, 043910 (2017).
- [29] Z. Yang, X. Lu, W. Tan, J. Zhao, D. Yang, Y. Yang, Y. He, and K. Zhou, XPS studies of nitrogen doping niobium used for accelerator applications, *Appl. Surf. Sci.* **439**, 1119 (2018).
- [30] Z. Yang, X. Lu, Y. He, W. Tan, S. Huang, and H. Guo, Magnetic properties and hydrides precipitation observation of

- nitrogen doping niobium used for accelerator applications, arXiv:1804.07443 (2018).
- [31] P. Dhakal, S. Chetri, S. Balachandran, P. J. Lee, and G. Ciovati, Effect of low temperature baking in nitrogen on the performance of a niobium superconducting radio frequency cavity, *Phys. Rev. Accel. Beams* **21**, 032001 (2018).
- [32] P. Dhakal, G. Ciovati, P. Kneisel, and G. R. Myneni, Enhancement in quality factor of SRF niobium cavities by material diffusion, *IEEE Trans. Appl. Supercond.* **25**, 1 (2015).
- [33] A. Grassellino, A. Romanenko, Y. Trenikhina, M. Checchin, M. Martinello, O. S. Melnychuk, S. Chandrasekaran, D. A. Sergatskov, S. Posen, A. C. Crawford, S. Aderhold, and D. Bice, Unprecedented quality factors at accelerating gradients up to  $45 \text{ MVm}^{-1}$  in niobium superconducting resonators via low temperature nitrogen infusion, *Supercond. Sci. Technol.* **30**, 094004 (2017).
- [34] G. Ciovati, G. Ereemeev, and F. Hannon, High field Q slope and the effect of low-temperature baking at 3 GHz, *Phys. Rev. Accel. Beams* **21**, 012002 (2018).
- [35] A. Gurevich, Reduction of Dissipative Nonlinear Conductivity of Superconductors by Static and Microwave Magnetic Fields, *Phys. Rev. Lett.* **113**, 087001 (2014).
- [36] A. Anthore, H. Pothier, and D. Esteve, Density of States in a Superconductor Carrying a Supercurrent, *Phys. Rev. Lett.* **90**, 127001 (2003).
- [37] K. Maki, The behavior of superconducting thin films in the presence of magnetic fields and currents, *Prog. Theor. Phys.* **31**, 731 (1964).
- [38] P. Fulde, Tunneling density of states for a superconductor carrying a current, *Phys. Rev.* **137**, A783 (1965).
- [39] K. Maki, in *superconductivity*, edited by R. D. Parks (Marcel Dekker, Inc., New York, 1969).
- [40] M. P. Garfunkel, Surface impedance of type-I superconductors: Calculation of the effect of a static magnetic field, *Phys. Rev.* **173**, 516 (1968).
- [41] A. Gurevich, Theory of RF superconductivity for resonant cavities, *Supercond. Sci. Technol.* **30**, 034004 (2017).
- [42] S. Casalbuoni, E. A. Knabbe, J. Kötzler, L. Lilje, L. von Sawilski, P. Schmüser, and B. Steffen, Surface superconductivity in niobium for superconducting RF cavities, *Nucl. Instrum. Meth. Phys. Res. A* **538**, 45 (2005).
- [43] T. Proslie, M. Kharitonov, M. Pellin, J. Zasadzinski, and G. Ciovati, Evidence of surface paramagnetism in niobium and consequences for the superconducting cavity surface impedance, *IEEE Trans. Appl. Supercond.* **21**, 2619 (2011).
- [44] A. Gurevich and T. Kubo, Surface impedance and optimum surface resistance of a superconductor with an imperfect surface, *Phys. Rev. B* **96**, 184515 (2017).
- [45] T. Kubo and A. Gurevich, Field-dependent nonlinear surface resistance and its optimization by surface nanostructuring in superconductors, *Phys. Rev. B* **100**, 064522 (2019).
- [46] A. Dacca, G. Gemme, L. Mattera, and R. Parodi, XPS analysis of the surface composition of niobium for superconducting RF cavities, *Appl. Surf. Sci.* **126**, 219 (1998).
- [47] K. Kowalski, A. Bernasik, W. Singer, X. Singer, and J. Camra, in *Proc. 11-th Workshop on RF Superconductivity* (Travemünde, Germany, 2003).
- [48] R. Cava, B. Batlogg, J. Krajewski, P. Gammel, H. Poulsen, W. Peck, and L. Rupp, Antiferromagnetism and metallic conductivity in  $\text{Nb}_{12}\text{O}_{29}$ , *Nature* **350**, 598 (1991).
- [49] R. Cava, B. Batlogg, J. Krajewski, H. Poulsen, P. Gammel, W. Peck, and L. Rupp, Electrical and magnetic properties of  $\text{Nb}_2\text{O}_{5-\delta}$  crystallographic shear structures, *Phys. Rev. B* **44**, 6973 (1991).
- [50] T. McQueen, Q. Xu, E. Andersen, H. Zandbergen, and R. Cava, Structures of the reduced niobium oxides  $\text{Nb}_12\text{O}_{29}$  and  $\text{Nb}_2\text{O}_{5.4}$ , *J. Solid State Chem.* **180**, 2864 (2007).
- [51] A. Romanenko and D. I. Schuster, Understanding Quality Factor Degradation in Superconducting Niobium Cavities at low Microwave Field Amplitudes, *Phys. Rev. Lett.* **119**, 264801 (2017).
- [52] W. P. M. R. Pathirana and A. Gurevich, Nonlinear dynamics and dissipation of a curvilinear vortex driven by a strong time-dependent Meissner current, *Phys. Rev. B* **101**, 064504 (2020).
- [53] N. R. Groll, C. Becker, G. Ciovati, A. Grassellino, A. Romanenko, J. F. Zasadzinski, and T. Proslie, Insight into bulk niobium superconducting RF cavities performances by tunneling spectroscopy, arXiv:1805.06359v1.
- [54] B. Aune *et al.*, Superconducting TESLA cavities, *Phys. Rev. ST Accel. Beams* **3**, 092001 (2000).
- [55] G. Ciovati, Ph.D. thesis, Phys. Dept., Old Dominion University, Norfolk, VA, USA, (2005).
- [56] The Stopping and Range of Ions in Matter. ver. SRIM-2013, 2013. [Online]. Available: <http://www.srim.org/>
- [57] M. Grundner and J. Halbritter, On the natural  $\text{Nb}_2\text{O}_5$  growth on Nb at room temperature, *Surf. Sci.* **136**, 144 (1984).
- [58] Z. P. Hu, Y. P. Li, M. R. Ji, and J. X. Wu, The interaction of oxygen with niobium studied by XPS and UPS, *Solid State Commun.* **71**, 849 (1989).
- [59] B. R. King, H. C. Patel, D. A. Gulino, and B. J. Tatarchuk, Kinetic measurements of oxygen dissolution into niobium substrates: In situ X-ray photoelectron spectroscopy studies, *Thin Solid Films* **192**, 351 (1990).
- [60] H. Tian, C. E. Reece, M. J. Kelley, S. Wang, L. Plucinski, K. E. Smith, and M. M. Nowell, Surface studies of niobium chemically polished under conditions for superconducting radio frequency (SRF) cavity production, *Appl. Surf. Sci.* **253**, 1236 (2006).
- [61] G. D. L. Semione, A. Dangwal Pandey, S. Tober, J. Pfrommer, A. Poulain, J. Drnec, G. Schütz, T. F. Keller, H. Noei, V. Vonk, B. Foster, and A. Stierle, Niobium near-surface composition during nitrogen infusion relevant for superconducting radio-frequency cavities, *Phys. Rev. Accel. Beams* **22**, 103102 (2019).
- [62] I. Lindau and W. E. Spicer, Oxidation of Nb as studied by the UV-photoemission technique, *J. Appl. Phys.* **45**, 3720 (1974).
- [63] H. H. Farrell, H. S. Isaacs, and M. Strongin, The interaction of oxygen and nitrogen with the niobium (100) surface: II. Reaction kinetics, *Surf. Sci.* **38**, 31 (1973).
- [64] R. Franchy, T. U. Bartke, and P. Gassmann, The interaction of oxygen with Nb (110) at 300, 80 and 20 K, *Surf. Sci.* **366**, 60 (1996).
- [65] S. Hashimoto and A. Tanaka, Alteration of Ti  $2p$  XPS spectrum for titanium oxide by low-energy Ar ion bombardment, *Surf. Interface Anal.* **34**, 262 (2002).
- [66] T. Ohsawa, J. Okubo, T. Suzuki, H. Kumigashira, M. Oshima, and T. Hitosugi, An n-type transparent

- conducting oxide: Nb<sub>12</sub>O<sub>29</sub>, *J. Phys. Chem. C* **115**, 16625 (2011).
- [67] J. Halbritter, On the oxidation and on the superconductivity of niobium, *Appl. Phys. A* **43**, 1 (1987).
- [68] P. C. Karulkar, Effects of sputtering on the surface composition of niobium oxides, *J. Vac. Sci. Technol.* **18**, 169 (1981).
- [69] J. Zasadzinski, in *The Physics of Superconductors*, edited by K. H. Bennemann and J. B. Ketterson (Springer, Berlin, Heidelberg, 2003), p. 591, Chap. 15.
- [70] R. C. Dynes, V. Narayanamurti, and J. Garno, Direct Measurement of Quasiparticle-Lifetime Broadening in a Strong-Coupled Superconductor, *Phys. Rev. Lett.* **41**, 1509 (1978).
- [71] W. Brinkman, R. Dynes, and J. Rowell, Tunneling conductance of asymmetrical barriers, *J. Appl. Phys.* **41**, 1915 (1970).
- [72] G. Blatter, M. V. Feigel'man, V. B. Geshkenbein, A. I. Larkin, and V. M. Vinokur, Vortices in high-temperature superconductors, *Rev. Mod. Phys.* **66**, 1125 (1994).
- [73] E. H. Brandt, The flux-line lattice in superconductors, *Rep. Prog. Phys.* **58**, 1465 (1995).
- [74] C. Caroli, P. G. De Gennes, and J. Matricon, Bound Fermion states on a vortex line in a type II superconductor, *Phys. Lett.* **9**, 307 (1964).
- [75] H. F. Hess, R. B. Robinson, R. C. Dynes, J. M. Valles, Jr., and J. V. Waszczak, Scanning-Tunneling-Microscope Observation of the Abrikosov Flux Lattice and the Density of States near and inside a Fluxoid, *Phys. Rev. Lett.* **62**, 214 (1989).
- [76] C. Renner, A. D. Kent, P. Niedermann, Ø. Fischer, and F. Lévy, Scanning Tunneling Spectroscopy of a Vortex Core from the Clean to the Dirty Limit, *Phys. Rev. Lett.* **67**, 1650 (1991).
- [77] R. P. Robertazzi, A. W. Kleinsasser, R. B. Laibowitz, R. H. Koch, and K. G. Stawiasz, *In situ* Ag/YBa<sub>2</sub>Cu<sub>3</sub>O<sub>7</sub> contacts for superconductor-normal-metal-superconductor devices, *Phys. Rev. B* **46**, 8456 (1992).
- [78] J. W. Ekin, S. E. Russek, C. C. Clickner, and B. Jeanneret, *In situ* noble metal YBa<sub>2</sub>Cu<sub>3</sub>O<sub>7</sub> thin-film contacts, *Appl. Phys. Lett.* **62**, 369 (1993).
- [79] V. S. Stolyarov, T. Cren, Ch. Brun, I. A. Golovchanskiy, O. V. Skryabina, D. I. Kasatonov, M. M. Khapaev, M. Yu. Kupriyanov, A. A. Golubov, and D. Roditchev, Expansion of a superconducting vortex core into a diffusive metal, *Nat. Commun.* **9**, 2277 (2018).
- [80] A. Gurevich, Tuning vortex fluctuations and the resistive transition in superconducting films with a thin overlayer, *Phys. Rev. B* **98**, 024506 (2018).